

Article

Synergistic Mechanism of Rare-Earth Modification TiO₂ and Photodegradation on Benzohydroxamic Acid

Chunying Wang ¹ , Ting Zeng ¹, Sipin Zhu ¹ and Chuantao Gu ^{1,2,*}

¹ College of Resource and Environmental Engineering, Jiangxi University of Science and Technology, Ganzhou 341000, China; cywang@jxust.edu.cn (C.W.); 15779716279@163.com (T.Z.); Zhusipin926@163.com (S.Z.)

² School of Chemistry and Chemical Engineering, Xiamen University, Xiamen 361005, China

* Correspondence: gctao@163.com; Tel.: +86-1517-071-1957

Received: 10 December 2018; Accepted: 11 January 2019; Published: 18 January 2019



Abstract: Rare earth elements are plentiful in Gannan area, China, and there is a large amount of wastewater from all kinds of mines. In this paper, rare-earth modification TiO₂ composites (RE/TiO₂, RE = La, Ce, Gd, Yb) was studied by theory computation and experimental performance. The prepared RE/TiO₂ was investigated for the degradation of benzohydroxamic acid (BHA) as a typical residual reagent in wastewater from beneficiation. The crystallinity, morphology, specific surface area, light absorption, and composition of compound were investigated by various techniques. As a result of computation and experimentation, four different electron configurations of rare earth all retained the anatase phase of TiO₂ and reduced the band gap of TiO₂ to some degree compared with pure TiO₂. Different rare-earth elements and calcination temperatures resulted in different removal effects on BHA. The optimum doping contents were 0.75% (500 °C), 0.20% (500 °C), 0.70% (500 °C) and 0.50% (450 °C) for La, Ce, Gd, Yb respectively. All the RE/TiO₂ composites studied in this research still possessed good photoactivity after four runs, which supports the theoretical and practical basement for the photocatalytic treatment of mining and metallurgy wastewater.

Keywords: rare-earth modification; theory computation; BHA; photocatalytic degradation

1. Introduction

Many organic reagents were used in the froth flotation during the ore-dressing. Some of them discharged with the wastewater and are harmful to aquatic organisms and humans. The reported research indicated that some deformed cells of algae (*Scenedesmus obliquus*) were found in cultures exposed to 0145 for 48 h [1]; most of the fishes would die while the concentration of xanthate was over 5.0 mg·L⁻¹ [2]; Acrylonitrile, as the synthetic raw material of Ester-105, is possibly carcinogenic to humans (Group 2B) [3]. Besides, the residual beneficiation reagents might induce the release of heavy metals from the tailings pond, resulting in secondary pollution [4].

Many methods have been developed to treat organic beneficiation reagents or other organic compounds such as physical adsorption [5], biodegradation [6] and chemical oxidation [7,8], and so on. For example, there needs to be 5 or more days to get to the removal efficiency of 85% for benzohydroxamic acid (BHA, the most widely-used collector in the flotation industry at present) with the method of biodegradation [9]. However, our previous studies indicated that La/TiO₂ and Yb/TiO₂ possessed high photodegradation activity to BHA (the removal efficiency was up to 90% in 2 h) [10]. TiO₂ has been considered as the most promising photocatalyst among various semiconductor photocatalyst materials due to its benign physicochemical property and low cost [11]. In recent years,

in order to improve the photocatalytic activity of TiO₂, the research topics have been aimed at resolving the problems of wide band gap (3.2 eV) and easy recombination of photogenerated electron-hole pairs. It is reported that doping with metal ions is an efficient way to enhance the photocatalytic activity of TiO₂ [12,13]. Rare-earth elements have been proved to effectively promote the activity of TiO₂ because of the 4f electronic structure [14–16]. Joanna reported that the sample of 1 mol% of Yb³⁺-TiO₂ showed the highest photoactivity on the degradation of phenol under the visible light ($\lambda > 450$ nm) irradiation in the form of anatase of TiO₂ [15]. Sun's research results demonstrated that Nd doping inhibited the growth of TiO₂ crystallite and enhanced the thermal stability of anatase TiO₂ [16]. One suggested theory about the promoted photoactivity of rare-earth element doped compounds is that: The existence of the ground and excited states of rare-earth elements could reduce the recombination of electron-hole pairs by the transformation between RE³⁺ and RE²⁺ [17,18]. Another proposed theory is that the added rare earth would change the surface composition of TiO₂ (more hydroxyl oxygen and adsorbed oxygen and some Ti³⁺ species existed at the surface of the rare-earth modified TiO₂ (RE/TiO₂) compared with pure TiO₂) [19,20]. Most of the published papers have focused on the discussion of RE/TiO₂ with one rare-earth element or two co-doped rare-earth elements [21–23]. Zhao Zongyan and Bian Liang calculated lanthanide-doped anatase/rutile TiO₂ by density functional theory (DFT) respectively [24,25], and the results indicated that most of the doped rare-earth ions could obviously reduce the band gap widths. To our knowledge, there is no systematic report of the combination of theoretical computation and practical experimentation.

In this study, La, Ce, Gd, and Yb were chosen to prepare the rare-earth-doped TiO₂ due to their different 4f and 5d orbits. The 4f and 5d orbitals are 4f⁰5d¹, 4f²5d⁰, 4f⁷5d¹, 4f¹⁴5d⁰ for La, Ce, Gd and Yb, respectively. So, La, Ce, Gd, Yb present the non-4f orbitals, normal-4f orbitals, semi-4f orbitals, and full-4f orbitals. The synthesized RE/TiO₂ composites were characterized by XRD, XPS, UV-vis DRS, and N₂ adsorption. Besides, the band structure and partial density of states (PDOS) of RE/TiO₂ were calculated by DFT. Beneficiation BHA was used to test the photodegradation activity of RE/TiO₂ compositions. What is more, the effects of RE doping amount, calcination temperature and the reusability of RE/TiO₂ were investigated. In a word, this paper studies and analyses the structure and photocatalytic activity of RE/TiO₂ on BHA by theoretical computation and practical experiment.

2. Materials and Methods

2.1. Materials

Tetrabutyl titanate and rare-earth nitrate were bought from National Medicine Group Chemical Reagent Co. Ltd., Shanghai, China. Acetic acid and absolute ethyl alcohol were bought from Tianjin Damao Chemical Reagent Factory, Tianjin, China. Benzohydroxamic acid was obtained from Western Mining co., LTD., Xining, China. All the reagents except BHA were used as received without any purification, and BHA was used after purification.

2.2. Preparation of RE/TiO₂

RE/TiO₂ were prepared by the sol-gel method according to previous research [10]. Rare-earth nitrate in the required stoichiometry was mixed with 2 mL deionized water, 2 mL acetic acid and 10 mL absolute ethanol, and the mixture solution after stirring was noted as solution A. Solution B was prepared with 10 mL tetrabutyl titanate and 15 mL absolute ethanol. Homogeneous and transparent sol was obtained after solution A was added dropwise to solution B under agitation. The continuous stirring of RE/TiO₂ produced the wet gel, and the xerogel was formed after aging at atmospheric temperature for 48 h and then drying at 90 °C. The synthetic product was crushed to get fine powder by agate mortar and calcined in a furnace (400 °C–600 °C). Finally, the RE/TiO₂ composites were achieved. The doped rare earth was set to 0~1.0% according to TiO₂ in mass.

2.3. Characterization of RE/TiO₂

Power X-ray diffraction (XRD) patterns were recorded by an X-ray diffractometer (Rigaku Miniflex, Japan) at 40 kV and 40 mA using monochromatized Cu K α radiation. Element constitutions and values of RE/TiO₂ were analyzed by the X-ray photoelectron spectroscopy (XPS) with a Thermo type multi-function imaging electronic spectrometer (ESCALAB 250XI, Thermo Fisher, Waltham, USA). A UV-vis spectrophotometer (UV-2550, Shimadzu, Tokyo, Japan) was used to determine the light absorption of RE/TiO₂. The Brunauer–Emmett–Teller (BET) surface areas and Nitrogen adsorption–desorption isotherms were measured by adsorption apparatus (ASAP 2460, Micromeritics, Norcross, GA, USA) at liquid nitrogen temperature (−196 °C).

2.4. Degradation of BHA by RE/TiO₂

The photocatalytic experiments were operated in a photochemical reactor. RE/TiO₂ was dispersed into a 50 mL BHA (30 mg/L) solution. In order to make sure of the adsorption–desorption equilibrium of BHA on RE/TiO₂, the reaction solution was stirred continuously without irradiation for 30 min. Then, the 300 W mercury light was turned on. Approximately 5 mL of suspension solution was sampled and centrifuged (10,000 r/min) at set time intervals and then was determined by UV-vis spectrophotometry at 229 nm. The removal rate (*R*) was determined as follows:

$$R(\%) = (c_0 - c_t) / c_0 \times 100\%, \quad (1)$$

where *C*₀ (mg/L) is the initial concentration of BHA and *C*_{*t*} (mg/L) is the concentration at reaction time *t* (min).

2.5. Recycle Test of RE/TiO₂

Batch experiments were conducted to invest the reusability of RE/TiO₂. In five quartz test tubes (No 1, 2, 3 and 4), 0.0500 g RE/TiO₂ was added followed by the addition of 50 mL of BHA aqueous solution at 20 mg/L. Before irradiation, the suspension was stirred in the dark for 30 min to establish adsorption–desorption equilibrium of BHA on the catalysts. Approximately 4 mL of aqueous sample was withdrawn from the tube of No 1 at certain time intervals of irradiation for analysis, and the reaction lasted for 120 min. For the other three test tubes, the reaction solution was centrifuged after 120 min of irradiation. The supernatant was removed and 50 mL of fresh BHA aqueous solution at 20 mg/L was added. Another 120 min of irradiation was continued. For the tubes of No 2, 3 and 4, the photodegradation was repeated for two, three and four runs, respectively.

2.6. Computational Parameters

The CASTEP module (MS2016) based on DFT [26] was used to calculate the band structure and PDOS of pure anatase TiO₂ and RE/TiO₂. For RE/TiO₂, a supercell of 2 × 2 × 1 48-atoms anatase TiO₂ was used, and one Ti atom near the center of the supercell was replaced by one rare-earth atom. The general gradient approximation (GGA) for the exchange–correlation term was employed, and the Perdew–Burke–Ernzerhof (PBE) scheme was adopted for structure optimization. Convergence of energy change per atom is at 5 × 10^{−6} eV; stress is at 0.02 GPa; residual force is at 0.01 eV/Å; and displacement of atoms is at 0.0005 Å. The self-consistent field (SCF) tolerance was adopted with the convergence of 1.0 × 10^{−7} eV/atom. The FFT grid of the basis was 50 × 50 × 64. The kinetic energy cutoff for the plane-waves basis was set to 400 eV. For the computation, 3 × 3 × 3 k-points used for sampling the Brillouin zone, and the ultrasoft pseudopotential were applied in the above calculation. The electronic configurations considered are 3s²3p⁶3d²4s² (Ti), 2s²2p⁴ (O), 5s²5p⁶5d¹6s² (La), 4f¹5s²5p⁶5d¹6s² (Ce), 4f⁷5s²5p⁶5d¹6s² (Gd) and 4f¹⁴ 5s²5p⁶6s² (Yb) for anatase TiO₂ (unit cell) and RE/TiO₂ (2 × 2 × 1 supercell) (Figure 1).

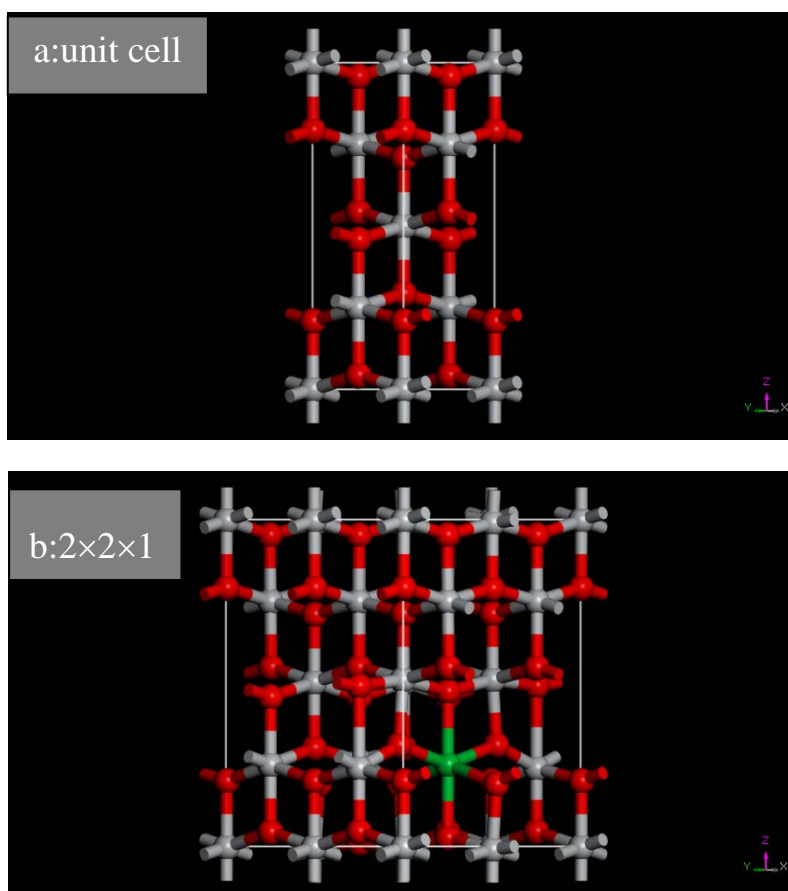


Figure 1. Pure anatase TiO₂ ((a), unit cell) and anatase RE/TiO₂ ((b), supercell). The red, gray and green spheres represent oxygen, titanium and rare-earth atoms, respectively.

3. Results and Discussions

3.1. Characterization

3.1.1. Texture Properties

As seen from Figure 2, XRD patterns of prepared pure TiO₂ and RE/TiO₂ were all in accordance with JCPDS Card No.21-1272 of anatase TiO₂ [27,28]. The characteristics peak of all RE/TiO₂ became broader and lower than pure TiO₂, suggesting a decrease in crystallite sizes (Table 1). The higher the rare-earth doping amount, the broader the XRD pattern peaks and the lower the intensity [29]. In other words, the doping of rare-earth elements slowed down the growth of TiO₂ nanoparticles, changed the surface structure of TiO₂ particles, and improved the diffusion barrier of TiO₂ grain.

Table 1. Crystallite sizes calculated by Scherrer formula.

Sample	Size (nm)	Sample	Size (nm)	Sample	Size (nm)	Sample	Size (nm)
Pure TiO ₂ (500 °C)	19.0	0.10%Ce/TiO ₂	16.5	0.10%Gd/TiO ₂	14.9	Pure TiO ₂ (450 °C)	14.2
0.25%La/TiO ₂	18.4	0.20%Ce/TiO ₂	13.3	0.20%Gd/TiO ₂	12.7	0.10%Yb/TiO ₂	11.9
0.50%La/TiO ₂	15.6	0.30%Ce/TiO ₂	13.1	0.30%Gd/TiO ₂	12.3	0.20%Yb/TiO ₂	11.7
0.75%La/TiO ₂	13.4	0.40%Ce/TiO ₂	12.5	0.50%Gd/TiO ₂	12.0	0.30%Yb/TiO ₂	11.2
1.00%La/TiO ₂	11.5	0.50%Ce/TiO ₂	12.4	0.70%Gd/TiO ₂	11.9	0.50%Yb/TiO ₂	11.1
				1.00%Gd/TiO ₂	11.5	0.70% b/TiO ₂	10.9
						1.00%Yb/TiO ₂	10.4

There are no new phases except anatase TiO₂ by XRD analysis for the doped catalyst. So, RE³⁺ might highly disperse on the surface or enter into the lattice of TiO₂. Therefore, the growth of TiO₂

particles was hindered by doped rare-earth elements. Besides, the rare-earth compounds might become light interception sub-trapping centers, which is important to retard the recombination of the electron-hole pairs and to affect the photodegradation activity [30].

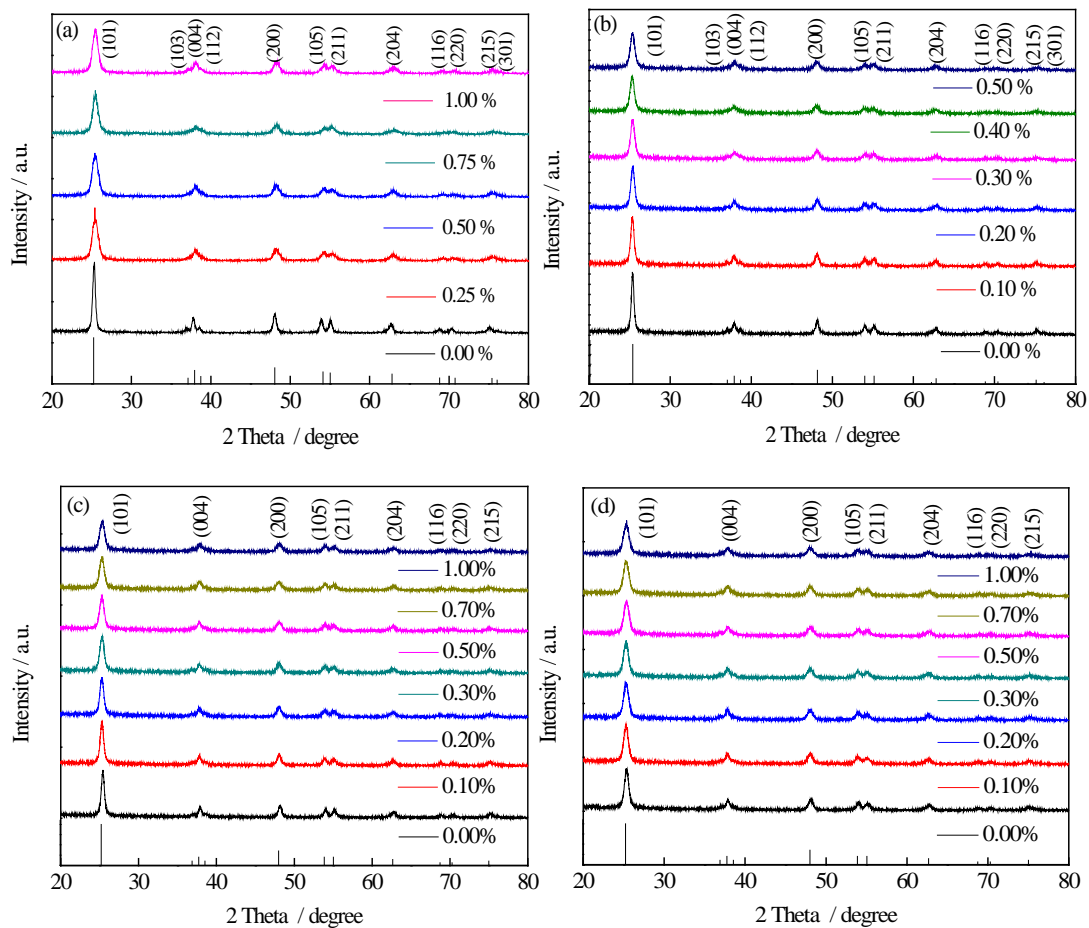


Figure 2. X-ray diffraction (XRD) patterns of RE/TiO₂ samples. (a) La/TiO₂ (500 °C); (b) Ce/TiO₂ (500 °C); (c) Gd/TiO₂ (500 °C); (d) Yb/TiO₂ (450 °C).

3.1.2. Optical Absorption Property

The UV-Vis DRS spectra of pure TiO₂ and RE/TiO₂ are presented in Figure 3. The band gap energy (E_g) was calculated by Formula (2) as follows [31]:

$$\alpha hv = A(hv - E_g)^{(n/2)}, \quad (2)$$

where α , h , v , and A represent the absorption coefficient, Planck's constant, light frequency and a constant respectively. The value of n is 4 as indirect transition for TiO₂.

By calculation, 0.75%La/TiO₂ (500 °C), 0.20%Ce/TiO₂ (500 °C), 0.70%Gd/TiO₂ (500 °C) and 0.50%Yb/TiO₂ (450 °C) have the most red-shift compared with pure TiO₂ in their own doped range, indicating a decrease in the band gap; the E_g were 3.17 eV, 2.93 eV, 3.10 eV and 3.16 eV respectively, while the E_g of pure TiO₂ was 3.21 eV and 3.20 eV for 500 °C and 450 °C, respectively. The red-shift could be attributed to the charge-transfer transition between 4f or 5d electrons of rare-earth elements and the conduction or valence band of TiO₂ due to the hybridization between the O 2p and RE 4f/5d orbitals after the RE element is substituted or interstitially incorporated into the TiO₂ lattice [32]. As discussed above, the doping of rare-earth elements reduced the band gap compared with pure TiO₂, and ultimately augments the photodegradation ability of RE/TiO₂ composites [33]. There is further

explanation about the effect of rare area earth elements on the band structure and hybridization of anatase TiO₂ in the computation section.

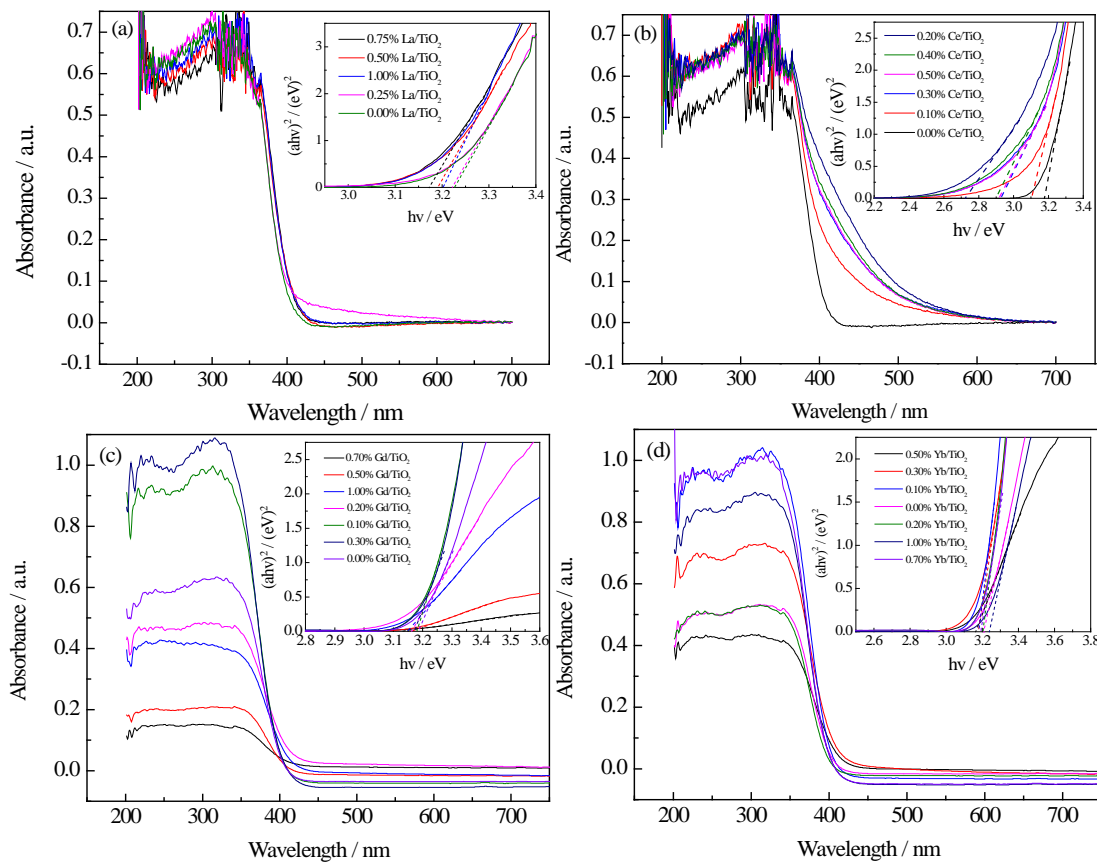


Figure 3. UV-Vis DRS patterns of RE/TiO₂ with different rare-earth doping ratios. (a) La/TiO₂; (b) Ce/TiO₂; (c) Gd/TiO₂; (d) Yb/TiO₂.

3.1.3. Composition and Chemical State Analysis

XPS was applied to analyse the composition and chemical state of pure TiO₂ and RE/TiO₂. Figure 4a indicates the survey spectra; there are obvious O and Ti peaks that come from synthesized pure TiO₂ or RE/TiO₂. Figure 4b indicates the spectra of doped La, and the characteristic peaks of La were detected near 853.92 eV and 836.79 eV, which suggests that rare-earth element La was doped successfully. However, the other three elements Ce, Gd and Yb were not detected by XPS. In order to prove the existence of Ce, Gd and Yb in the prepared RE/TiO₂, EDS was used to analyze the content. The result indicates that there was 0.016% of Ce in 0.20%Ce/TiO₂, 0.20% of Yb in 0.5% Yb/TiO₂, and 0.40% of Gd in 0.70% Gd/TiO₂.

The peaks of Ti2p and O1s for pure TiO₂ and Gd/TiO₂ were analyzed as shown in Figure 4c–f. Ti peaks of pure TiO₂ are located at 464.45 eV and 458.74 eV while Ti peaks of Gd/TiO₂ are located at 464.48 eV and 458.76 eV. The peak of O1s was fitted into two peaks: crystal lattice oxygen and hydroxyl oxygen [11]. The fitted peak of O1s at 529.83 eV corresponded to the lattice oxygen while the peak at 530.31 eV corresponded to hydroxyl oxygen for pure TiO₂. As seen from Figure 4c–f, after doping with Gd, the binding energy of Ti2p increased while the binding energy of O1s decreased for Gd/TiO₂ compared with pure TiO₂. The other three RE/TiO₂ composites (La/TiO₂, Ce/TiO₂ and Yb/TiO₂) all present a similar situation, which might be due to the interaction of RE with Ti and O in RE/TiO₂ [34].

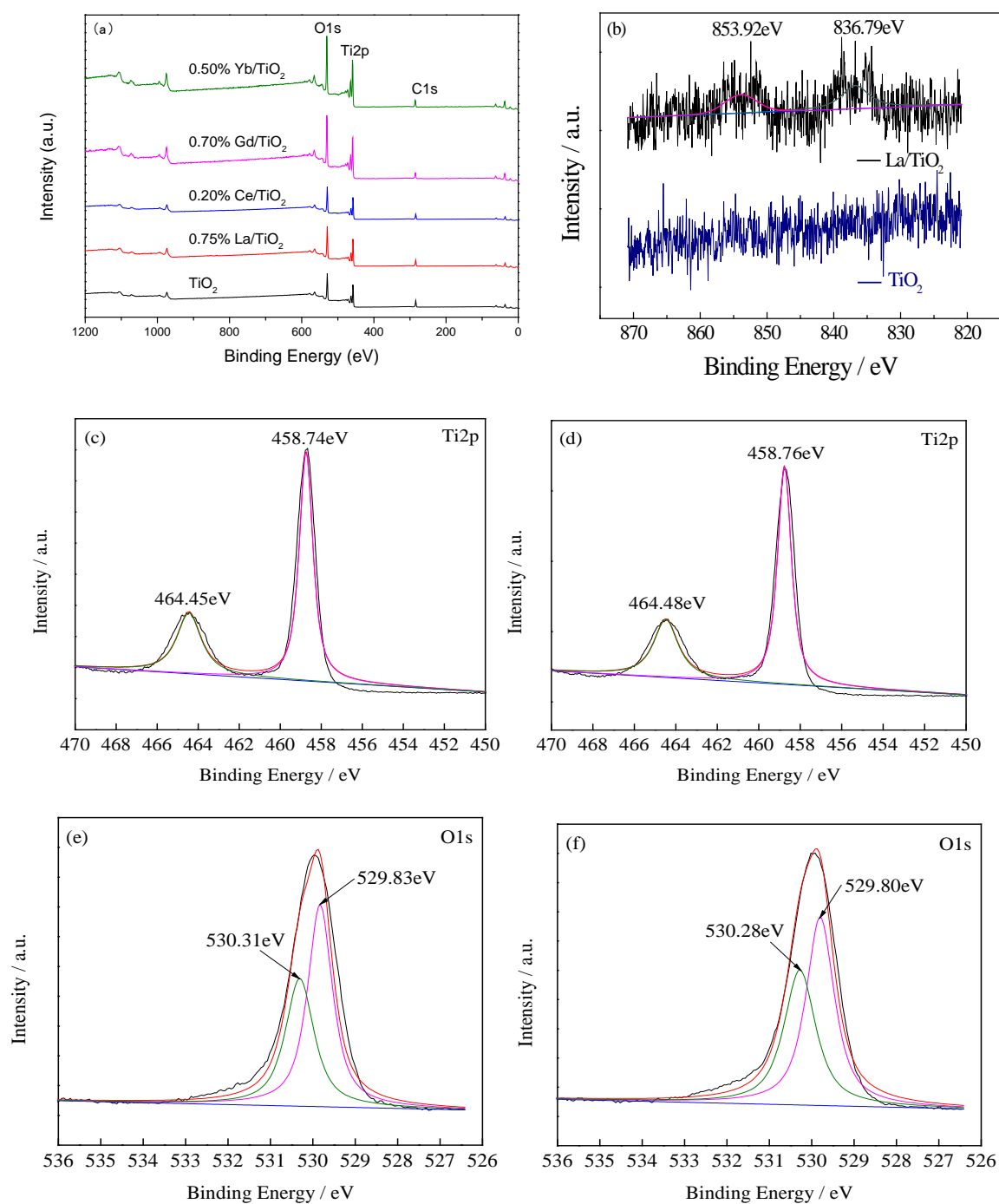


Figure 4. X-ray photoelectron spectroscopy (XPS) of RE/TiO₂. (a) Full XPS scan of RE/TiO₂; (b) La3d; (c) Ti2p in pure TiO₂; (d) Ti2p in Gd/TiO₂ (e) O1s in pure TiO₂; (f) O1s in Gd/TiO₂.

3.1.4. Analysis of S_{BET} and Pore Size Distribution

As seen from Figure S1 of the N₂ adsorption–desorption isotherms, all prepared RE/TiO₂ present the mesoporous structure [35,36]. The hysteresis loops of pure TiO₂ and RE/TiO₂ are consistent with type H2 that has uniform particle accumulation on the hole. The shape of the holes is considered to be a bottle-shaped channel of small mouth and large cavity, like an ink [14]. Besides, the distribution of pore size ranges from 2 nm to 10 nm, which belongs to the mesoporous pore. The S_{BET} was 39.39, 41.19, 40.42, 91.84, 86.78, and 113.89 m²/g for pure TiO₂ (500 °C), 0.75%La/TiO₂ (500 °C), 0.20%Ce/TiO₂ (500 °C), 0.70%Gd/TiO₂ (500 °C), pure TiO₂ (450 °C), and 0.50%Yb/TiO₂ (450 °C) respectively. Obviously,

all the S_{BET} of RE/TiO₂ composites are larger than that of pure TiO₂ calcined at the same temperature, especially for Gd and Yb doped TiO₂, which is in accordance with analysis result of XRD. The result may be owing to the linkage between the rare-earth ions and titanium by the oxygen bridge, which could effectively increase the specific surface area of TiO₂ [37].

3.2. Computation and Analysis

Table 2 shows the lattice parameters of pure TiO₂ and RE/TiO₂. Parameters *a* and *b* almost have no changes compared to pure TiO₂ ($2 \times 2 \times 1$ supercell), while the *c* is longer than pure TiO₂, resulting in the increase of cell volume (the radius of La³⁺, Ce³⁺, Gd³⁺, and Yb³⁺ is larger than Ti⁴⁺). The result is inconsistent with the reference's calculation [23,24].

Table 2. Lattice parameters of rare-earth-doped anatase TiO₂.

	<i>a</i> /nm	<i>b</i> /nm	<i>c</i> /nm	<i>V</i> /nm ³
TiO ₂ (unit cell)	3.8064	3.8064	9.6716	140.13
TiO ₂ ($2 \times 2 \times 1$ supercell)	7.6126	7.6126	9.6710	560.46
La/TiO ₂ ($2 \times 2 \times 1$ supercell)	7.5917	7.5919	10.3202	594.81
Ce/TiO ₂ ($2 \times 2 \times 1$ supercell)	7.6552	7.6555	9.9428	582.66
Gd/TiO ₂ ($2 \times 2 \times 1$ supercell)	7.6386	7.6502	9.9168	579.48
Yb/TiO ₂ ($2 \times 2 \times 1$ supercell)	7.6290	7.6291	9.9296	577.93

The calculated result indicates the indirect band gap of 2.105 eV for anatase TiO₂ (unit cell), which is significantly lower than the laboratory data (approximately 3.2 eV). However, the electronic structure is essentially the same [24]. The band gaps of calculated doped TiO₂ are 1.951 eV, 2.059 eV, 0.475 eV, and 2.029 eV for La/TiO₂, Ce/TiO₂, Gd/TiO₂, and Yb/TiO₂ (Figure 5), respectively, all less than pure anatase TiO₂, which is in agreement with the laboratory result in the study. Gd/TiO₂ has the biggest changes on band gap according to the poor stability of Gd's electrons. According to Bian's statement, the energy state forms of RE dopants inside the CB and VB are divided into three parts including deep impurity states (electron transfer from RE energy state to CB), shallow impurity states (electron transfer from VB to RE energy state) and both states [25]. It could be concluded that element Yb belongs to deep impurity states, La and Ce belong to shallow impurity states, and Gd belongs to both.

Similar to the pure anatase TiO₂, there also exists the hybridization of O 2p and Ti 3d states in the valence band region for RE/TiO₂ observed from the calculated PDOS (Figure S2). As seen from Figure 6, there exists impurity energy localized at about 0.743 eV above the Fermi level for Gd/TiO₂ ($2 \times 2 \times 1$ supercell), which indicates that some of the Gd 4f states are partially occupied. Simultaneously, the formation of Gd-O bonds leads to the partial hybridization of the Gd 4f orbitals with O 2p states below the Fermi level (Figure 6b). Therefore, the introduced Gd 4f orbital mainly contributes to extend the impurities' energy level into the forbidden band and produce a wider valence band in comparison with the pure TiO₂. Besides, the top of the valence band shifts obviously while the bottom of the conduction band shifts slightly with respect to the Fermi level, which results in the narrower band gap and the consequent redshift response of the optical absorption edge [38].

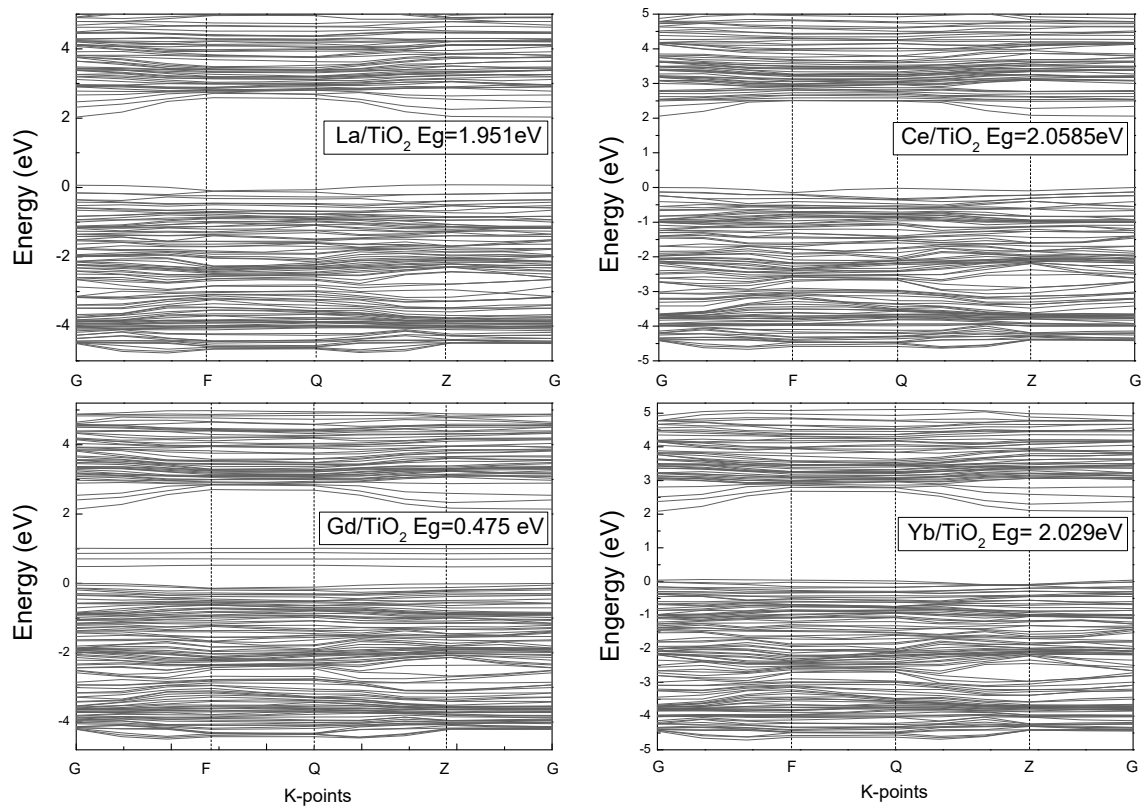


Figure 5. Band structure of RE/TiO₂ (2 × 2 × 1 supercell).

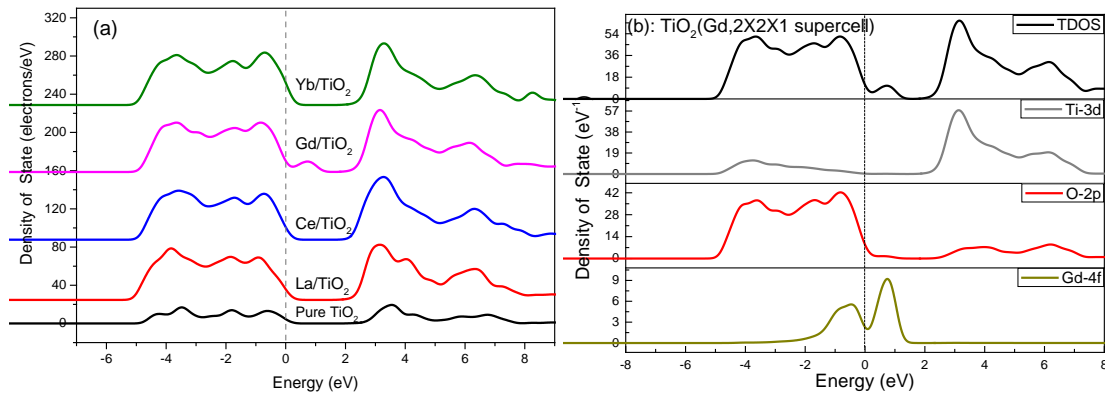


Figure 6. TDOS of RE/TiO₂ (2 × 2 × 1 supercell) (a) and PDOS (b) of Gd/TiO₂ (2 × 2 × 1 supercell).

3.3. Photodegradation on BHA

3.3.1. Effect of Doped Amount of Rare Earth

Different rare-earth elements and doped amounts affected the photocatalytic activity of RE/TiO₂ on BHA. As shown in Figure 7, the removal efficiency of BHA by direct photolysis was very low and the adsorption ability of RE/TiO₂ to BHA was negligible. Compared with pure TiO₂, La and Ce indicate significant effects on BHA photodegradation while Gd and Yb only have tiny promoted effects on the photodegradation. Along with the overall trend, the photocatalytic activity of RE/TiO₂ on BHA enhanced with the increased amount of doped rare-earth element and then was weakened with the further increased amount, especially for La and Ce doped composites. In a word, the photodegradation ability of 0.75%La/TiO₂, 0.20%Ce/TiO₂, 0.70%gd/TiO₂, and 0.50%Yb/TiO₂ are up to the highest compared with pure TiO₂ or other kinds of the same doped materials, which are in consistence with the analysis of UV-Vis DRS.

The addition of rare earth would result in expanding the lattice of TiO_2 , which has been proved by computation. The expansion might lead to crystal defects and distortion, ultimately affecting the energy band structure and weakening the recombination of photogenerated electrons and holes. However, too many defects would become the recombination center if excess rare-earth element was doped. So, there always exists an optimum doped amount [39].

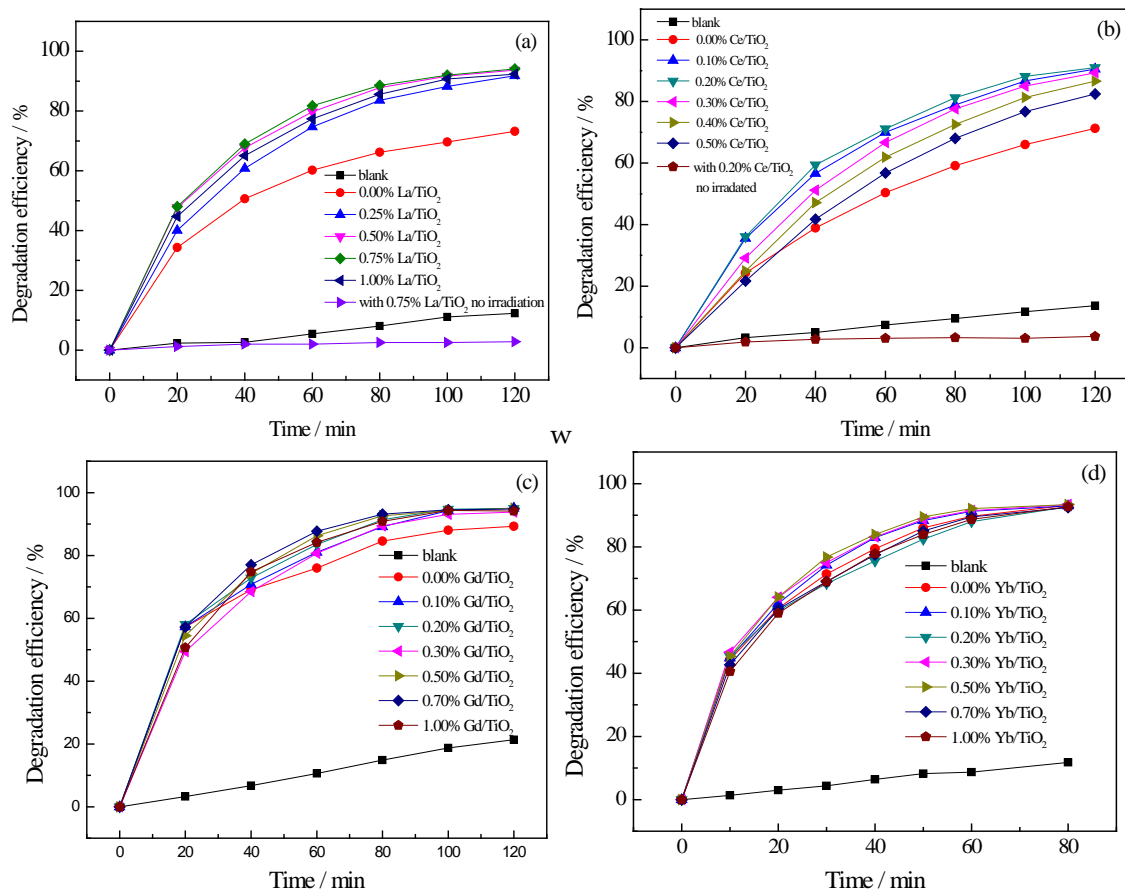


Figure 7. Effects of doping amount of RE/ TiO_2 on the photodegradation of benzohydroxamic acid (BHA). (a) La/ TiO_2 (500 °C); (b) Ce/ TiO_2 (500 °C); (c) Gd/ TiO_2 (500 °C); (d) Yb/ TiO_2 (450 °C).

3.3.2. Effect of Calcination Temperature

Different calcination temperature would result in different morphology of prepared materials, ultimately affecting the photodegradation activity of catalysts. As seen from Figure 8, 500 °C was the appropriate temperature for 0.75%La/ TiO_2 , 0.20%Ce/ TiO_2 and 0.70%Gd/ TiO_2 while 450 °C was the appropriate temperature for 0.50%Yb/ TiO_2 . As we know, the material prepared at a low temperature would have a low crystallization degree and have a large amount of recombination centers for photogenerated electrons and holes. However, the excessive sinter would cause the agglomeration of catalyst particles or transform the phase of TiO_2 from anatase to rutile, leading to the lower photocatalytic activity. According to the published reports, the anatase form of TiO_2 always had higher photocatalytic ability [14,15]. As a result, it could be concluded that rare-earth elements and calcination temperature both affect the photodegradation of BHA.

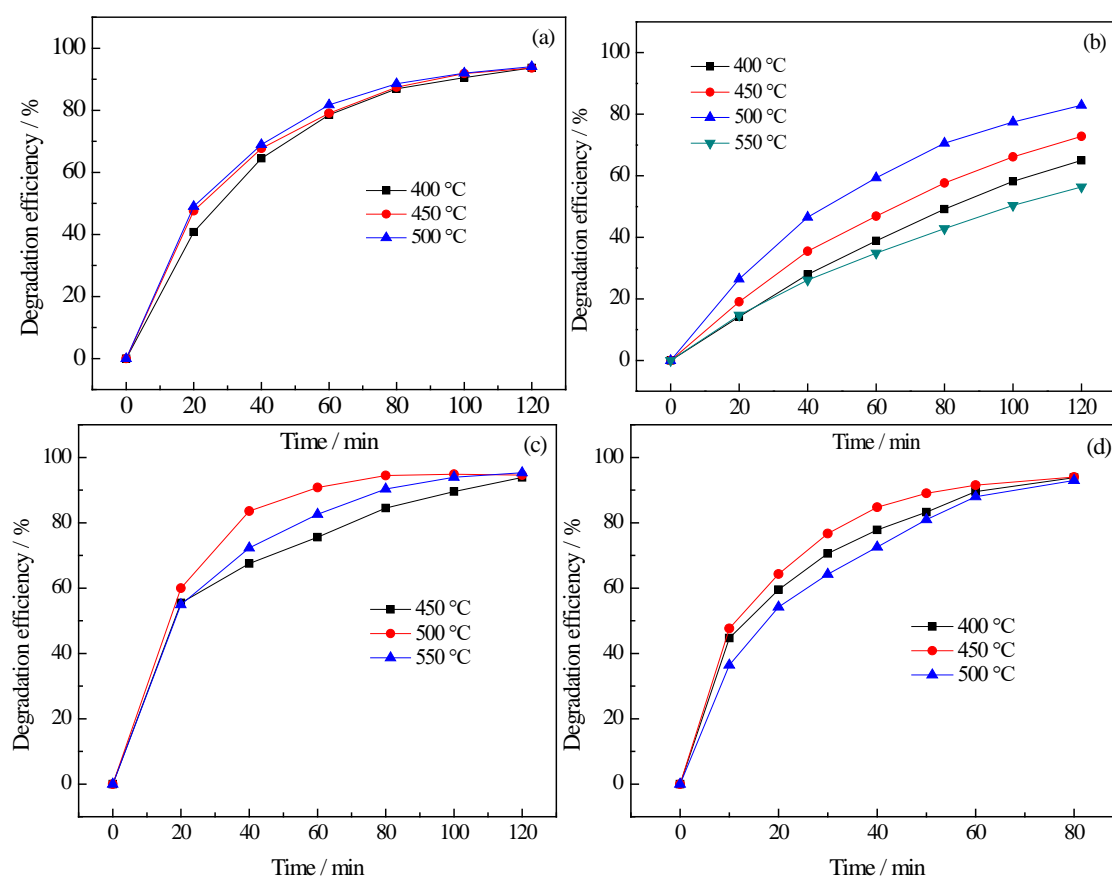


Figure 8. Effect of calcination temperatures on the photodegradation of BHA by RE/TiO₂. (a) 0.75%La/TiO₂; (b) 0.20%Ce/TiO₂; (c) 0.70%Gd/TiO₂; (d) 0.50%Yb/TiO₂.

3.3.3. Stability of RE/TiO₂

Reusability is an important indicator in evaluating the photocatalyst except for their photoactivity in the practical application. RE/TiO₂ composites were used four times to test their reusability on the photodegradation of BHA. As seen in Figure 9, during the last three runs, the removal rate only decreased about 0.8%~3.4% compared with the first run, which indicates that RE/TiO₂ continuously keeps the good photodegradation effect on BHA, and confirms the potential ability in engineering applications.

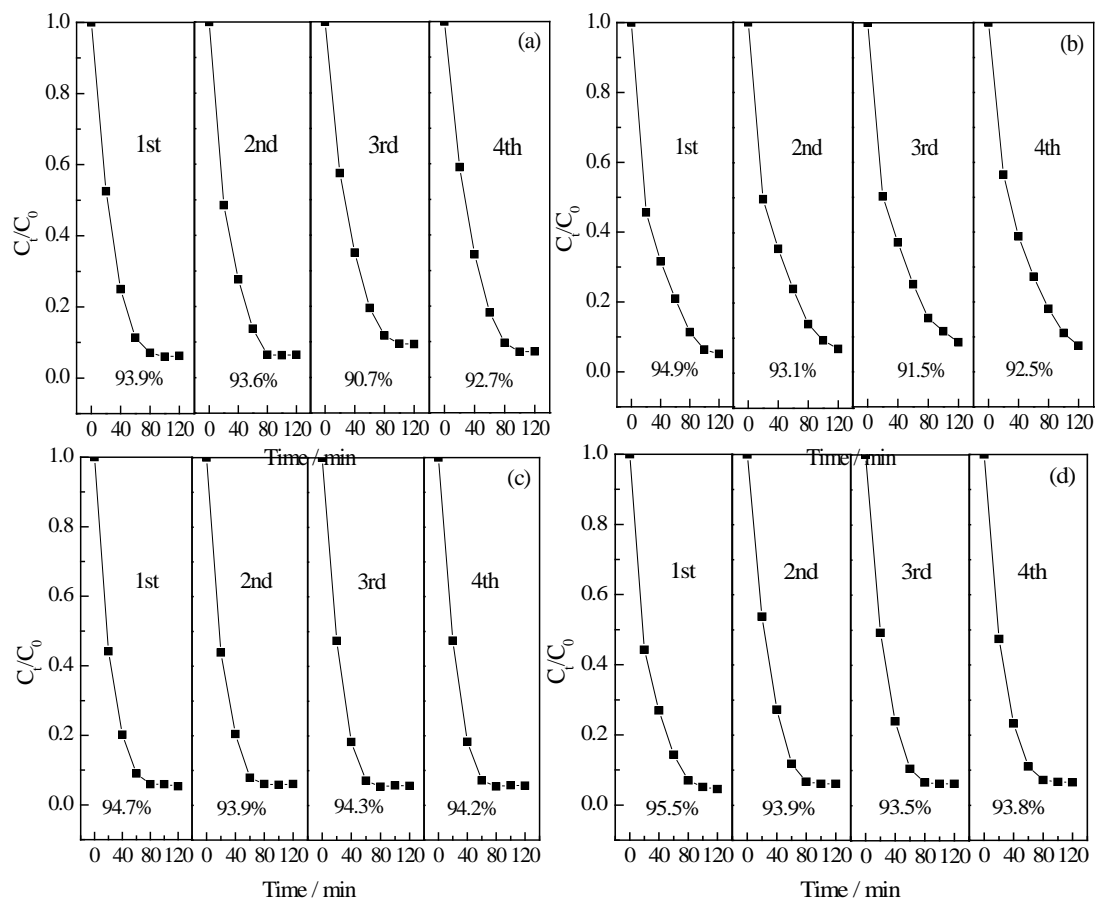


Figure 9. Recycling test of RE/TiO₂ for photocatalytic degradation of BHA. (a) 0.75%La/TiO₂; (b) 0.20%Ce/TiO₂; (c) 0.70%Gd/TiO₂; (d) 0.50%Yb/TiO₂.

4. Conclusions

RE/TiO₂ composites were prepared successfully by a simple Sol-Gel method. Four rare-earth elements La, Ce, Gd, and Yb might highly disperse on the surface or enter into the lattice of TiO₂ and hinder the growth of TiO₂ particles. Due to the linkage between the rare-earth ions and titanium by the oxygen bridge, the specific surface area of RE/TiO₂ composites was effectively increased. Besides, the rare-earth compounds might become light interception sub-trapping centers and reduce the band gap compared with pure TiO₂, which is important to retard the recombination of the electron-hole pairs and ultimately affect the photodegradation activity of the composites. The photodegradation experiment indicates that the doped rare-earth elements could enhance the removal efficiency of BHA from beneficiation wastewater. Each rare-earth element had its own optimum doped amount, and the optimum doping contents were 0.75%La/TiO₂, 0.20%Ce/TiO₂, 0.70%gd/TiO₂, and 0.50%Yb/TiO₂ for La, Ce, Gd, and Yb doped composites respectively. The calculated result is basically in line with the experiment. However, there exists a big difference in the band gap between the experiment and computation because of the different ratio for Gd/Ti. Four types of RE/TiO₂ all demonstrate the high photocatalytic activity and excellent reusability for BHA after four runs.

Supplementary Materials: The following are available online at <http://www.mdpi.com/2076-3417/9/2/339/s1>, Figure S1: N₂ adsorption-desorption isotherms and pore size distributions (inset) of pure TiO₂ (a,e) and RE/TiO₂ (b–f). (a) Pure TiO₂ (500 °C); (b) 0.75% La/TiO₂ (500 °C); (c) 0.20% Ce/TiO₂ (500 °C); (d) 0.70% Gd/TiO₂ (500 °C); (e) Pure TiO₂ (450 °C); (f) 0.50% Yb/TiO₂ (450 °C). Figure S2: TDOS and PDOS of anatase TiO₂ (unit cell) and RE/TiO₂ (2 × 2 × 1 supercell, La/TiO₂, Ce/TiO₂, Yb/TiO₂).

Author Contributions: Conceptualization, C.W.; software, C.G.; investigation, T.Z. and S.Z.; data curation, S.Z.; writing—original draft preparation, C.W.; writing—review and editing, C.G.

Funding: This research was funded by the National Natural Science Foundation of China (21408277), China Postdoctoral Science Foundation (2016T90967, 2015M582776XE).

Acknowledgments: This work was supported by Academic and Technical Leaders of the Main Disciplines in Jiangxi Province, and Program of Qingjiang Excellent Young Talents, JXUST.

Conflicts of Interest: The authors declare no conflict of interest.

References

1. Qijun, K.; Yizheng, X. Comparison of the toxicities of six mine floatation agents to algae. *Acta Hydrobiol. Sin.* **1992**, *16*, 245–250. (In Chinese)
2. Yan, H.; Lian, W.X. Degradation and influence factors of ammonium butyl aerofloat in paddy soil. *Acta Sci. Circumst.* **2012**, *32*, 1454–1458. (In Chinese)
3. International Agency for Research on Cancer. Re-evaluation of some organic chemicals, hydrazine and hydrogen peroxide (Part 1, Part 2, Part 3). In *IARC Monographs on the Evaluation of Carcinogenic Risks to Humans*; World Health Organization: Lyon, France, 1999; Volume 71, pp. 43–108.
4. Schaidler, L.A.; Senn, D.B. Characterization of Zinc, Lead, and Cadmium in Mine Waste: Implications for Transport, Exposure, and Bioavailability. *Environ. Sci. Technol.* **2007**, *41*, 4164–4171. [[CrossRef](#)] [[PubMed](#)]
5. Ayranci, E.; Conway, B.E. Adsorption and electrosorption of ethyl xanthate and thiocyanate anions at high-Area carbon-cloth electrodes studied by in situ UV spectroscopy: Development of procedures for wastewater purification. *Anal. Chem.* **2001**, *73*, 1181–1189. [[CrossRef](#)]
6. Natarajan, K.A.; Prakasan, M.R.S. Biodegradation of sodium isopropyl xanthate by *Paenibacillus polymyxa* and *Pseudomonas putida*. *Miner. Metall. Process.* **2013**, *30*, 226–232. [[CrossRef](#)]
7. Guo, Y.; Cui, K. Fe(III) ions enhanced catalytic properties of $(\text{BiO})_2\text{CO}_3$ nanowires and mechanism study for complete degradation of xanthate. *Chemosphere* **2017**, *181*, 190–196. [[CrossRef](#)]
8. Pinho, L.; Hernández-Garrido, J.C. 2D and 3D characterization of a surfactant-synthesized $\text{TiO}_2\text{-SiO}_2$ mesoporous photocatalyst obtained at ambient temperature. *Phys. Chem. Chem. Phys.* **2013**, *15*, 2800–2808. [[CrossRef](#)]
9. Wenjun, Z. *Study on the Biodegradability of Hydroxamic Acid Collectors*; Wuhan University of Technology: Wuhan, China, 2012.
10. Luo, X.; Wang, J. Degradation and mineralization of benzohydroxamic acid by synthesized mesoporous La/TiO_2 . *Int. J. Environ. Res. Public Health* **2016**, *13*, 997. [[CrossRef](#)]
11. Lyu, J.; Gao, J. Construction of homojunction-adsorption layer on anatase TiO_2 to improve photocatalytic mineralization of volatile organic compounds. *Appl. Catal. B Environ.* **2017**, *202*, 664–670. [[CrossRef](#)]
12. He, D.; Huang, X. Synthesis and catalytic performance of Yb^{3+} , Er^{3+} doped titanium dioxide. *Asian J. Chem.* **2015**, *27*, 1477–1480. [[CrossRef](#)]
13. Saqib, N.U.; Adnan, R. A mini-review on rare earth metal-doped TiO_2 for photocatalytic remediation of wastewater. *Environ. Sci. Pollut. Res.* **2016**, *23*, 15941–15951. [[CrossRef](#)] [[PubMed](#)]
14. Lara-López, Y.; García-Rosales, G. Synthesis and characterization of carbon- $\text{TiO}_2\text{-CeO}_2$ composites and their applications in phenol degradation. *J. Rare Earth.* **2017**, *35*, 551–558. [[CrossRef](#)]
15. Reszczyńska, J.; Grzyb, T. Visible light activity of rare earth metal doped (Er^{3+} , Yb^{3+} or $\text{Er}^{3+}/\text{Yb}^{3+}$) titania photocatalysts. *Appl. Catal. B Environ.* **2015**, *163*, 40–49. [[CrossRef](#)]
16. Sun, D.; Wang, K. Synthesis and photocatalytic activity of sulfate modified Nd-doped TiO_2 under visible light irradiation. *J. Rare Earth.* **2015**, *33*, 491–497. [[CrossRef](#)]
17. Devi, L.G.; Kumar, S.G. Exploring the critical dependence of adsorption of various dyes on the degradation rate using $\text{Ln}^{3+}\text{-TiO}_2$ surface under UV/solar light. *Appl. Surf. Sci.* **2012**, *261*, 137–146. [[CrossRef](#)]
18. Samadi, M.; Zirak, M. Recent progress on doped ZnO nanostructures for visible-light photocatalysis. *Thin Solid Films* **2016**, *605*, 2–19. [[CrossRef](#)]
19. Li, J.; Yang, X. Rare earth oxide-doped titania nanocomposites with enhanced photocatalytic activity towards the degradation of partially hydrolysis polyacrylamide. *Appl. Surf. Sci.* **2009**, *255*, 3731–3738. [[CrossRef](#)]
20. Liu, H.; Yu, L. The progress of TiO_2 nanocrystals doped with rare earth ions. *J. Nanomater.* **2012**, *2012*, 13.
21. Chai, Y.; Lin, L. Efficient visible-light photocatalysts from Gd-La codoped TiO_2 nanotubes. *Ceram. Int.* **2014**, *40*, 2691–2696. [[CrossRef](#)]

22. Zhang, W.; Yu, N. Synthesis of Yb³⁺/Er³⁺ co-doped Bi₂WO₆ nanosheets with enhanced photocatalytic activity. *Mater. Lett.* **2016**, *163*, 16–19. [[CrossRef](#)]
23. Trujillo-Navarrete, B.; del Pilar Haro-Vázquez, M. Effect of Nd³⁺ doping on structure, microstructure, lattice distortion and electronic properties of TiO₂ nanoparticles. *J. Rare Earth.* **2017**, *35*, 259–270. [[CrossRef](#)]
24. Zhao, Z.; Liu, Q. Effects of lanthanide doping on electronic structures and optical properties of anatase TiO₂ from density functional theory calculations. *J. Phys. D Appl. Phys.* **2008**, *41*, 085417. [[CrossRef](#)]
25. Bian, L.; Song, M. Band gap calculation and photo catalytic activity of rare earths doped rutile TiO₂. *J. Rare Earths* **2009**, *27*, 461–468. [[CrossRef](#)]
26. Clark Stewart, J.; Segall Matthew, D. First principles methods using CASTEP. *Z. Kristallogr. Cryst. Mater.* **2005**, *220*, 567–570.
27. Ren, C.; Wang, G.; Chen, Y.; Chen, Y. Degradation of benzene on Zr-doped TiO₂ photocatalysts with a bimodal pore size distribution. *Rare Met.* **2014**, *33*, 714–722. [[CrossRef](#)]
28. Fan, W.-Q.; Bai, H.-Y.; Zhang, G.-H.; Yan, Y.-S.; Liu, S.-B.; Shi, W.-D. Titanium dioxide macroporous materials doped with iron: Synthesis and photo-catalytic properties. *CrystEngComm* **2014**, *16*, 116–122. [[CrossRef](#)]
29. Khalid, N.R.; Ahmed, E. Co-doping effect of carbon and yttrium on photocatalytic activity of TiO₂ nanoparticles for methyl orange degradation. *J. Ovonic Res.* **2015**, *11*, 107–112.
30. Liang, C.H.; Li, F.B. The enhancement of adsorption and photocatalytic activity of rare earth ions doped TiO₂ for the degradation of Orange I. *Dyes Pigments* **2008**, *76*, 477–484. [[CrossRef](#)]
31. Spadavecchia, F.; Cappelletti, G. Solar photoactivity of nano-N-TiO₂ from tertiary amine: Role of defects and paramagnetic species. *Appl. Catal. B Environ.* **2010**, *96*, 314–322. [[CrossRef](#)]
32. Liew, S.L.; Zhang, Z. Yb-doped WO₃ photocatalysts for water oxidation with visible light. *Int. J. Hydrog. Energy* **2014**, *39*, 4291–4298. [[CrossRef](#)]
33. Huang, F.; Guo, Y. Solgel-hydrothermal synthesis of Tb/Tourmaline/TiO₂ nano tubes and enhanced photocatalytic activity. *Solid State Sci.* **2017**, *64*, 62–68. [[CrossRef](#)]
34. Wand, C.; Li, Y. Synthesis, characterisation and photocatalytic activity of natural zeolite supported Fe/S and Cr/S codoped nano TiO₂ photocatalysts. *Mater. Technol.* **2014**, *29*, 372–376.
35. Wu, X.; Fang, S. Thiourea-modified TiO₂ nanorods with enhanced photocatalytic activity. *Molecules* **2016**, *21*, 181. [[CrossRef](#)] [[PubMed](#)]
36. Das, S.K.; Bhunia, M.K. Synthesis, characterization, and biofuel application of mesoporous zirconium oxophosphates. *ACS Catal.* **2011**, *1*, 493–501. [[CrossRef](#)]
37. Reszczynska, J.; Grzyb, T. Photocatalytic activity and luminescence properties of RE³⁺-TiO₂ nanocrystals prepared by sol-gel and hydrothermal methods. *Appl. Catal. B Environ.* **2016**, *181*, 825–837. [[CrossRef](#)]
38. Wei, Z.-N.; Jia, C.-L. First-principle calculations of the electronic and optical properties of Tm-doped anatase titanium dioxide. *Optice* **2015**, *54*, 037107. [[CrossRef](#)]
39. Irie, H.; Watanada, Y. Nitrogen-concentration dependence on photocatalytic activity of TiO₂-xNx powders. *J. Phys. Chem. B* **2003**, *107*, 5483–5486. [[CrossRef](#)]

